Normal Mode Analysis of the Linear Viscoelastic Response of Dissipative Systems: Application to Vertex Model

Sijie Tong,[1] Rastko Sknepnek,[2,3,*] and Andrej Košmrlj[1,4,†]

[1] *Department of Mechanical and Aerospace Engineering, Princeton University, Princeton, New Jersey 08544, USA*
[2] *School of Science and Engineering, University of Dundee, Dundee DD1 4HN, United Kingdom*
[3] *School of Life Sciences, University of Dundee, Dundee DD1 5EH, United Kingdom*
[4] *Princeton Institute of Materials, Princeton University, Princeton, New Jersey 08544, USA*

(Dated: February 8, 2022)

We present a semi-analytical method based on normal modes to calculate the dynamic linear viscoelastic properties of soft systems with various forms of dissipation. Each normal mode responds with a characteristic relaxation timescale, and their rheological behavior can be represented with the standard linear solid model. The method is applied to explore the linear shear rheology of the vertex model over a broad range of frequencies, which has been widely used to describe the mechanical properties of epithelial tissues. The analytical predictions are validated by the numerical simulation results for the vertex model using several different dissipation mechanisms mimicking several possible biological scenarios. This work provides insight of the connection between the dynamical modes and rheological properties of soft materials and biological tissues.

arXiv:2202.03261v1 [cond-mat.soft] 7 Feb 2022

I. INTRODUCTION

Soft materials exhibit rich mechanical and rheological behaviors such as viscoelasticity, time-dependent viscosity, shear thickening and thinning, etc. [1, 2]. Understanding these behaviors is of both fundamental and practical interest with many soft materials being ubiquitous in everyday life. Rich macroscopic rheological properties result from typically complex amorphous microscopic structure, relatively weak (i.e., often comparable with the thermal energy) interactions between constitutive elements, and dissipation. In polymer melts, for example, the storage modulus has a characteristic plateau over a range of frequencies due to very different time scales associated with the diffusion along and perpendicular to the polymer chain [3]. In dense emulsions, the loss modulus remains constant under oscillatory shear for driving frequencies as low as $10^{-2} - 1$ Hz [4], in contradiction to the linear response theory which predicts that the loss modulus is an odd function of frequency, and, therefore, should vanish for at low frequencies. This behavior is attributed to slow "glassy" dynamics [5, 6]. In granular media approaching the unjamming transition, the density of vibrational states remains constant at low frequencies leading to a diverging length scale [7], which results in scaling behavior of elasticity, transport, and force propagation as the packing fraction approaches the critical value [8–10].

Mechanical and rheological properties of living matter shares a lot in common with inanimate soft amorphous materials. There are, however, key differences. Most notably, biological systems are kept out of equilibrium by internal active processes and can tune their properties in response to chemical and mechanical changes in the environment. Living systems also grow, age, regenerate, etc. Epithelial tissues and monolayers, in particular, are typical examples of dense soft active matter [11] and have been known to show complex collective behaviors [12–16] with dynamical patterns reminiscent of supercooled liquids and active nematics [17–20]. There has, therefore, been growing interest in studying viscoelastic response of epithelia [21], which revealed complex non-linear behavior and led to interesting theoretical models, e.g., the description based on fractional derivatives [22, 23].

Understanding full non-linear response of soft and biological matter is faced with major challenges such as multiple competing length and time scales, irreversible plastic microscopic rearrangements that produce non-local stresses [24], aging, etc. Despite many theoretical and numerical studies of various aspects of the non-linear response, a general framework is still lacking. In the linear regime, however, many of these challenges can be neglected making a comprehensive treatment possible. The linear response treatment is clearly inadequate if one is interested in, as it is often the case, the long-time behaviors under large deformations. It can, nonetheless, provide valuable insights into often complex baseline behaviors of the system. Polymer melts provide an excellent, widely studied example [3].

In this paper we develop a semi-analytic formalism for exploring the linear rheological response of broad class of soft and biological matter over the full dynamic range. Our approach is based on the well-known expansion in terms of normal modes. We show that each normal mode is equipped with a characteristic relaxation timescale, and their rheological behavior can be represented with the standard linear solid model. Approximating the response of a many-body system to small perturbations by expanding around a local energy minimum in terms of mutually decoupled normal modes has been extensively used throughout physics, with modeling phonons in crys-

* r.sknepnek@dundee.ac.uk
† andrej@princeton.edu

tals being a textbook example [25].

The method discussed in this paper is general and it can be applied to any system that can be described by a smooth energy functional with well-defined local minima. It shares similarities with the method of Pessot, et al. [26] for calculating dynamic moduli in magnetic gels, but it is more general since it allows treatment of various dissipative mechanisms. In order to showcase its power, we applied it to study the linear response of the vertex model [27–29], widely used to describe mechanical properties of epithelial tissues. Using the vertex model, Bi, et al. [30] predicted that epithelial tissues can undergo rigidity transition at constant density by tuning cell properties. This unexpected results has been observed in-vitro in human bronchial cell monolayers [31], and has sparked interest in understanding how biological systems can take advantage of the presence of phase transitions and the accompanying tissue rheology [32, 33]. Understanding mechanical and rheological properties of the vertex model and the closely related self-propelled Voronoi model [34–36] has, therefore, attracted a lot of attention [37–40]. Given that the vertex model predicts the rigidity transition, it is natural to ask what happens to the response close this transition. Most studies to date [40–42], however, focused on large deformations in the quasistatic regime where plastic relaxation facilitated by cell rearrangements via T1 events leads to a strong non-linear response. Here, we take the opposite limit and explore the linear response of the vertex model over a wide range of frequencies and three different microscopic dissipation models. Our findings show that even in the linear regime, the vertex model shows complex viscoelastic response, especially in the fluid phase, with multiple competing time scales, which can be accurately represented with normal modes.

The paper is organized as follows. In Sec. II, we use the normal mode analysis to derive the linear response rheological properties of overdamped soft materials with both external and internal friction. In Sec. III, we apply this method to the vertex model of epithelial tissues and explicitly discuss three microscopic mechanisms of dissipation: 1) drag on a vertex due to cell-substrate interaction; 2) internal dissipation due to relative motion of neighboring vertices, and 3) internal dissipation due to relative motion of neighboring cells. The first model is suitable for studies of cell monolayers supported by a solid substrate while the later two are more appropriate for systems such as embryos. Finally, in Sec. IV, we summarize main results and briefly discuss advantages and limitations of our approach.

II. NORMAL MODE ANALYSIS

We model a soft viscoelastic system as a collection of N interacting agents (e.g., vertices of a network, colloids in a colloidal dispersion, cells in a tissue, etc.) whose interaction is described by a potential energy $E(\{\mathbf{R}_j\})$, where $\{\mathbf{R}_j\}$ denotes the set of position vectors of all agents in a suitably chosen reference frame. The position vector of agent j is $\mathbf{R}_j \in \mathbb{R}^d$ with d being the number of spacial dimensions and $j \in \{1, \ldots, N\}$. In general, the potential energy can be multi-body, and each agent i experiences the force $-\nabla_{\mathbf{R}_i} E(\{\mathbf{R}_j\})$. To simplify the notation, we introduce the column vector $\mathbf{r} \equiv (\mathbf{R}_1, \ldots, \mathbf{R}_N)$, which contains positions of all agents, i.e., $\mathbf{r} \in \mathbb{R}^{dN}$. Similarly, a $dN-$dimensional vector $-\nabla_{\mathbf{r}} E(\mathbf{r})$ represents forces acting on all agents. Since typical systems of interests are in the overdamped regime, the relaxation dynamics of the system in the absence of external driving force is described as

$$\hat{\boldsymbol{C}}\dot{\mathbf{r}}(t) = -\nabla_{\mathbf{r}} E(\mathbf{r}), \tag{1}$$

where the symmetric matrix $\hat{\boldsymbol{C}}$ provides generalization of the single friction coefficient to more complex mechanisms of energy dissipation.

We are interested in the linear response of the system around an equilibrium state $\mathbf{r}^{\mathrm{eq}}$, which corresponds to

$$\nabla_{\mathbf{r}} E\big|_{\mathbf{r}=\mathbf{r}^{\mathrm{eq}}} = 0. \tag{2}$$

In order to probe the linear response, we consider an external driving force $\mathbf{f}(t)$ that is sufficiently weak to produce deformations that are small compared to the typical distance between agents. The corresponding displacements are $\delta\mathbf{r} = \mathbf{r} - \mathbf{r}^{\mathrm{eq}}$ and linearized equations of motion take the form

$$\hat{\boldsymbol{C}}\delta\dot{\mathbf{r}}(t) = -\hat{\boldsymbol{H}}\delta\mathbf{r}(t) + \mathbf{f}(t), \tag{3}$$

where $\hat{\boldsymbol{H}}$ is the Hessian matrix with elements

$$\hat{H}_{ij} = \left.\frac{\partial^2 E}{\partial x_i \partial x_j}\right|_{\mathbf{r}=\mathbf{r}^{\mathrm{eq}}}. \tag{4}$$

x_i and x_j are, respectively, the i^{th} and j^{th} entries in the vector $\mathbf{r}$. Recall that $\hat{\boldsymbol{H}}$ is a real $dN \times dN$ symmetric matrix. If $\mathbf{r}^{\mathrm{eq}}$ corresponds to a true local energy minimum, then $\hat{\boldsymbol{H}}$ is positive definite. Here, we'll relax this condition and assume that $\hat{\boldsymbol{H}}$ is positive semi-definite, i.e., we will allow for the possibility that zero-energy modes are present in the system. Furthermore, in general, matrices $\hat{\boldsymbol{H}}$ and $\hat{\boldsymbol{C}}$ do not commute.

In order to solve Eq. (3), we consider the following generalized eigenvalue problem [43],

$$\hat{\boldsymbol{H}}\boldsymbol{\xi}_k = \lambda_k \hat{\boldsymbol{C}}\boldsymbol{\xi}_k, \tag{5}$$

where λ_k and $\boldsymbol{\xi}_k$ are the k^{th} eigenvalue and eigenvector, respectively. Since $\hat{\boldsymbol{H}}$ and $\hat{\boldsymbol{C}}$ are real symmetric matrices, the eigenvectors form a complete orthonormal basis $\mathcal{B} = \{\boldsymbol{\xi}_i | i = 1, \ldots, N\}$, i.e., $\langle \boldsymbol{\xi}_i, \boldsymbol{\xi}_j \rangle_{\hat{\boldsymbol{C}}} = \delta_{ij}$, where δ_{ij} is the Kronecker delta and the inner product is defined as $\langle \mathbf{u}, \mathbf{v} \rangle_{\hat{\boldsymbol{C}}} \equiv \mathbf{u}^{\intercal}\hat{\boldsymbol{C}}\mathbf{v}$. We can expand the displacement $\delta\mathbf{r}$ in the basis $\mathcal{B}$ as

$$\delta\mathbf{r}(t) = \sum_k a_k(t)\boldsymbol{\xi}_k, \tag{6}$$

where $a_k(t)$ is the amplitude of mode $\boldsymbol{\xi}_k$. Equations of motion of the system can then be projected along each normal mode. Since normal modes are orthogonal to each other and, hence, decoupled, each behaves as an independent harmonic oscillator with a spring constant λ_k. The projection, therefore, leads to a set of decoupled dynamical equations for the amplitudes a_k of normal modes,

$$\dot{a}_k(t) = -\lambda_k a_k(t) + f_k(t), \tag{7}$$

where $f_k(t) = \boldsymbol{\xi}_k^{\intercal}\mathbf{f}(t)$. We immediately see that λ_k^{-1} is the characteristic relaxation time of the normal mode k. For a given driving force $f_k(t)$, Eq. (7) can be solved as

$$a_k(t) = a_k(0)e^{-\lambda_k t} + \int_0^t dt' f_k(t')e^{-\lambda_k(t-t')}. \tag{8}$$

Thus, once the external driving force $\mathbf{f}(t)$ is specified, the dynamics of the system is fully determined by Eqs. (6)-(8). Finally, Eq. (7) has a simple solution in the frequency domain

$$\tilde{a}_k(\omega) = \frac{\tilde{f}_k(\omega)}{\lambda_k + i\omega}, \tag{9}$$

where the Fourier transform is defined as $\tilde{g}(\omega) = \int_{-\infty}^{+\infty} dt\, g(t)e^{-i\omega t}$.

A. Linear shear rheology of 2d systems with periodic boundaries

As an example of the general formalism presented above, we now demonstrate how to extract linear shear rheological properties of a $d = 2$–dimensional system with periodic boundary conditions. In numerical experiments, it is convenient to apply external driving via a macroscopic affine deformation of the entire system and measure the stress response in the system [44, 45]. In real systems, this could be achieved by placing the system on a sticky substrate and applying oscillatory shear deformation to the substrate. Due to the binding and unbinding of adhesive molecules, deformation of the system follows the deformation of the substrate on short timescales, but the system can relax and produce non-affine motion on longer timescales.

The affine deformation can be described as $\mathbf{R}_i(t) = \hat{\boldsymbol{F}}(t)\mathbf{R}_i^0$ where initial position $\mathbf{R}_i^0 \equiv \mathbf{R}_i(t=0)$ of agent i is mapped to the current position $\mathbf{R}_i(t)$ by an affine deformation gradient tensor $\hat{\boldsymbol{F}}(t)$ [46]. For instance, the shear rheology of the system can be probed by applying an oscillatory affine simple shear described by the deformation gradient tensor

$$\hat{\boldsymbol{F}} = \begin{pmatrix} 1 & \epsilon(t) \\ 0 & 1 \end{pmatrix}, \tag{10}$$

where $\epsilon(t) = \epsilon_0 \sin(\omega_0 t)$ is the applied shear strain with amplitude $\epsilon_0 \ll 1$. When the external driving is applied by imposing an affine deformation, the force balance in Eq. (1) needs to be modified as

$$\hat{\boldsymbol{C}}\left(\dot{\mathbf{r}}(t) - \mathbf{v}^{\text{aff}}(t)\right) = -\nabla_{\mathbf{r}} E\left(\mathbf{r}, \epsilon(\mathbf{t})\right), \tag{11}$$

since the dissipative forces are generated due to the relative motion between the system and the substrate [45]. Here, vector $\mathbf{v}^{\text{aff}}(t)$ contains the velocities of all agents due to the affine transformation, i.e., $\mathbf{v}^{\text{aff}} \equiv \left(\mathbf{V}_1^{\text{aff}}, \ldots, \mathbf{V}_N^{\text{aff}}\right)$, where $\mathbf{V}_i^{\text{aff}} = \left(\frac{d}{dt}\hat{\boldsymbol{F}}(t)\right)\mathbf{R}_i^0$ is the affine velocity of each individual agent. For the applied simple shear deformation in Eq. (10), the affine velocity of agent i is $\mathbf{V}_i^{\text{aff}} = (\dot{\epsilon}(t)R_i^{0,y}, 0)$, where $R_i^{0,y}$ is the $y-$coordinate of the agent i in the initial position.

It is important to note that for systems with periodic boundary conditions, the energy function of the system, $E\left(\mathbf{r}, \epsilon(\mathbf{t})\right)$, also depends on the applied shear strain $\epsilon(t)$. This dependence enters via the x-component of the separation distance R_{ij}^x between the agents i and j as $R_{ij}^x = R_j^x - R_i^x + q_{ij}^x \ell_x + \epsilon(t) q_{ij}^y \ell_y$ [36]. Here, R_i^x and R_j^x are the x-coordinates of the agents i and j, respectively, ℓ_x and ℓ_y are the sizes of the rectangular simulation box in the x and y directions, respectively. $q_{ij}^y = 0$ if agents i and j are connected without crossing the top or the bottom boundary and $q_{ij}^y = +1$ ($q_{ij}^y = -1$) if the bond connecting agent i to agent j crosses the top (bottom) boundary, with analogous expressions for q_{ij}^x in terms of the left and right boundaries [36].

Due to the dependence of the energy function $E\left(\mathbf{r}, \epsilon(\mathbf{t})\right)$ on the applied shear strain $\epsilon(t)$, the linearized equations of motion in Eq. (11) around the equilibrium state $\mathbf{r}^{\text{eq}}$ become

$$\hat{\boldsymbol{C}}\delta\dot{\mathbf{r}}(t) = -\hat{\boldsymbol{H}}\delta\mathbf{r}(t) + \overline{\mathbf{f}}^{\text{pb}}\epsilon(t) + \hat{\boldsymbol{C}}\mathbf{u}^{\text{aff}}\dot{\epsilon}(t). \tag{12}$$

Here, we introduced $\overline{\mathbf{f}}^{\text{pb}} = -\frac{\partial^2 E}{\partial \mathbf{r}\partial\epsilon}\Big|_{\mathbf{r}=\mathbf{r}^{\text{eq}},\epsilon=0}$ and rewritten the affine velocity as $\mathbf{v}^{\text{aff}} = \mathbf{u}^{\text{aff}}\dot{\epsilon}(t)$, where $\mathbf{u}^{\text{aff}} = \left(\mathbf{U}_1^{\text{aff}}, \ldots, \mathbf{U}_N^{\text{aff}}\right)$ with $\mathbf{U}_i^{\text{aff}} = (R_i^{0,y}, 0)$. As discussed above, the displacements can be expanded in the basis of normal modes as in Eq. (6). In this basis, the equations of motions in Eq. (12) become

$$\dot{a}_k(t) = -\lambda_k a_k(t) + \alpha_k \epsilon(t) + \beta_k \dot{\epsilon}(t), \tag{13}$$

where $\alpha_k = \boldsymbol{\xi}_k^{\intercal}\overline{\mathbf{f}}^{\text{pb}}$, $\beta_k = \langle \boldsymbol{\xi}_k, \mathbf{u}^{\text{aff}} \rangle_{\hat{\boldsymbol{C}}} = \boldsymbol{\xi}_k^{\intercal}\hat{\boldsymbol{C}}\mathbf{u}^{\text{aff}}$. The solution of Eq. (13) in the frequency domain is

$$\tilde{a}_k(\omega) = \left(\frac{\alpha_k + i\omega\beta_k}{\lambda_k + i\omega}\right)\tilde{\epsilon}(\omega). \tag{14}$$

In the linear response regime, the stress of the system due to external driving force is described by the stress tensor $\hat{\boldsymbol{\sigma}}(t)$ that can be written as a linear superposition of the stress tensor $\hat{\boldsymbol{\sigma}}_{\text{pb}}(t) = \epsilon(t)\hat{\boldsymbol{\sigma}}_{\text{pb}}^{\text{lin}}$ due to the shear of the periodic boundary and stress tensors $\hat{\boldsymbol{\sigma}}_k(t) = a_k(t)\hat{\boldsymbol{\sigma}}_k^{\text{lin}}(t)$ due to the motion along each mode k. Therefore, (see also Fig. 1)

$$\hat{\boldsymbol{\sigma}}(t) = \epsilon(t)\hat{\boldsymbol{\sigma}}_{\text{pb}}^{\text{lin}} + \sum_k a_k(t)\hat{\boldsymbol{\sigma}}_k^{\text{lin}}. \tag{15}$$

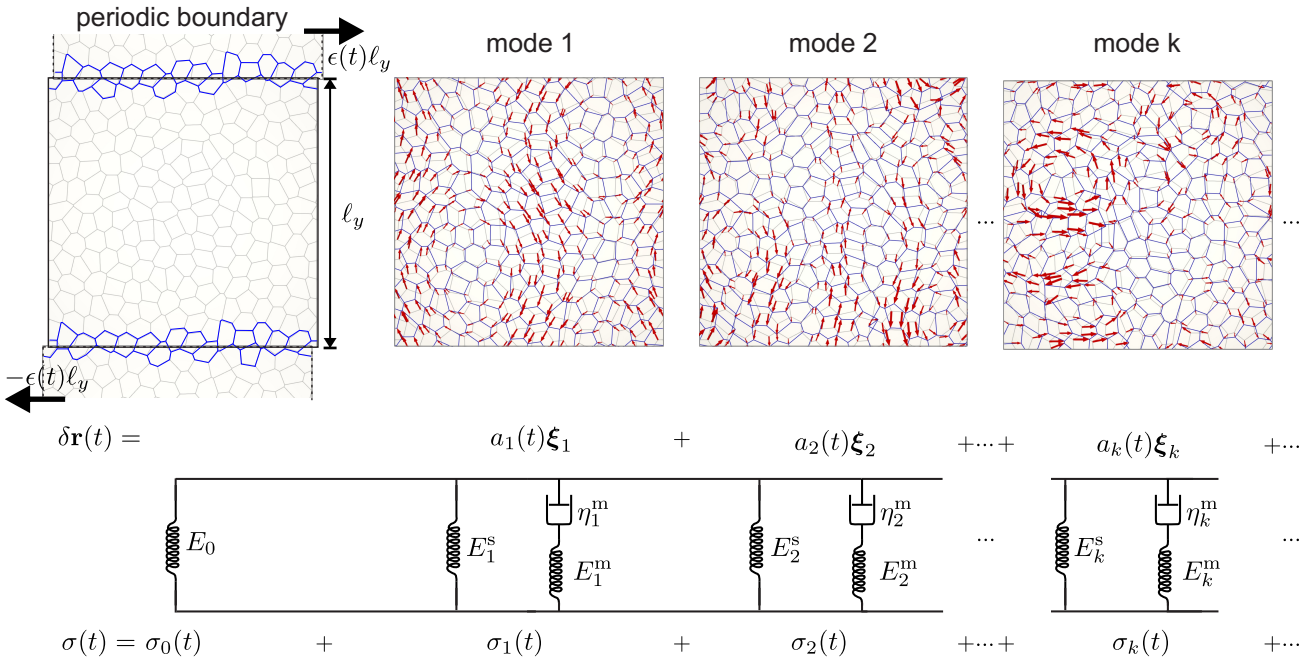

FIG. 1. A schematic of the decomposition of the motion and the response stress along normal modes. The plots on the top show the deformation due to the shear of the periodic boundary and representative normal modes for the vertex model. The grey mesh is the equilibrium configuration, red arrows show displacements associated with the normal mode $\boldsymbol{\xi}_k$, and the blue mesh is the configuration after displacing vertices in the direction of the normal mode. Similarly, in the top left panel blue cells indicate the distorted cells due to the shear of the periodic boundary. The displacement perturbed away from the equilibrium state $\delta\mathbf{r}$ can be written as a linear superposition of displacements along the normal modes $\boldsymbol{\xi}_k$. The stress response of the system [see Eq. (17)] due to shear deformation can be represented as a parallel sequence of a spring due to shear of the periodic boundary and standard linear solid (SLS) model elements, where each SLS model element describes the shear response of a normal mode. Values of spring constants and dashpot viscosities for normal mode model are given in text.

The linear response tensor $\hat{\boldsymbol{\sigma}}^{\mathrm{lin}}_{\mathrm{pb}}$ can be calculated by applying a small shear $\delta\epsilon_0 \ll 1$ to the periodic boundary, and measuring the resulting stress $\delta\hat{\boldsymbol{\sigma}}_{\mathrm{pb}}$ so that $\hat{\boldsymbol{\sigma}}^{\mathrm{lin}}_{\mathrm{pb}} = \delta\hat{\boldsymbol{\sigma}}_{\mathrm{pb}}/\delta\epsilon_0$. The linear response tensor $\hat{\boldsymbol{\sigma}}^{\mathrm{lin}}_k$ for mode k can be calculated by measuring the response stress tensor $\delta\hat{\boldsymbol{\sigma}}_k$ due to perturbation $\delta\mathbf{r} = \delta a\boldsymbol{\xi}_k$ along mode k so that $\hat{\boldsymbol{\sigma}}^{\mathrm{lin}}_k = \delta\hat{\boldsymbol{\sigma}}_k/\delta a$, where the amplitude δa is sufficiently small to produce deformations that are small compared to the typical distance between agents.

For the shear rheology, the dynamic shear modulus is defined as [1]

$$G^*(\omega) = \frac{\tilde{\hat{\sigma}}_{xy}(\omega)}{\tilde{\epsilon}(\omega)} = G_{\mathrm{pb}} + \sum_k \left(\frac{\alpha_k + i\omega\beta_k}{\lambda_k + i\omega}\right) G_k, \quad (16)$$

where $G_{\mathrm{pb}} \equiv \hat{\sigma}^{\mathrm{lin}}_{\mathrm{pb},xy}$ is the shear modulus due to the shear of the periodic boundary and $G_k \equiv \hat{\sigma}^{\mathrm{lin}}_{k,xy}$. In general, the dynamic shear modulus $G^*(\omega) = G'(\omega) + iG''(\omega)$ has a real part G', which is called the storage modulus, and an imaginary part G'', which is called the loss modulus [1]. Using Eq. (16), one can write the storage and loss moduli as

$$G'(\omega) = G_{\mathrm{pb}} + \sum_k G_k \left(\frac{\alpha_k\lambda_k + \beta_k\omega^2}{\lambda_k^2 + \omega^2}\right), \quad (17a)$$

$$G''(\omega) = \sum_k G_k \left(\frac{(-\alpha_k + \beta_k\lambda_k)\omega}{\lambda_k^2 + \omega^2}\right). \quad (17b)$$

Upon a closer look at the above expressions for the storage and loss moduli, we can recognize that each mode k behaves as a standard linear solid [1], and can be represented as a spring with elastic constant $E_k^{\mathrm{s}} = G_k\alpha_k/\lambda_k$ connected in parallel with a Maxwell element that consists of a spring $E_k^{\mathrm{m}} = G_k(-\alpha_k+\beta_k\lambda_k)/\lambda_k$ and a dashpot $\eta_k^{\mathrm{m}} = G_k(-\alpha_k+\beta_k\lambda_k)/\lambda_k^2$ connected in series. The characteristic time scale for mode k is $\eta_k^{\mathrm{m}}/E_k^{\mathrm{m}} = 1/\lambda_k$. The full rheological response of the system can thus be represented as a spring of elastic constant G_{aff} due to affine deformation and a sequence of standard linear solid elements connected in parallel, each corresponding to the contribution from one normal mode (see Fig. 1). The dynamic response of the system is thus characterized by a spectrum of timescales λ_k^{-1} corresponding to normal modes.

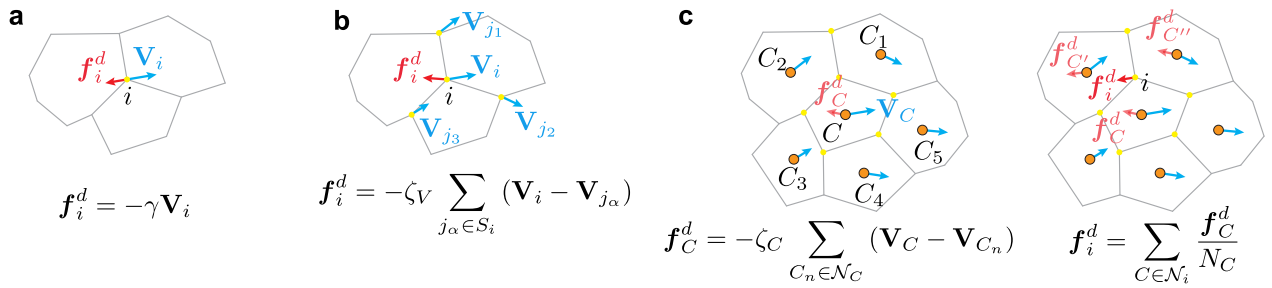

FIG. 2. Schematics of the three types of dissipation considered in this paper for the vertex model. Velocity vectors are shown in blue and friction force vectors are red. (a) The simplest model of dissipation for cells supported by a solid substrate. Vertex i experiences a frictional force proportional to its velocity $\mathbf{V}_i$, with friction coefficient γ. (b) Friction force on the vertex i is due to its motion relative to neighboring vertices. $\mathcal{S}_i$ is the "star" of vertex i, i.e., all vertices connected to vertex i. (c) Dissipation is due to the relative motion of neighboring cells. $\mathcal{N}_C$ includes all neighboring cells of cell C. $\mathcal{N}_i$ includes all cells that share vertex i. $\mathbf{f}_C^d$ is the friction force that cell C experiences due to relative motion with respect to its neighboring cells. $\mathbf{f}_i^d$ is the total friction force applied at vertex i. N_C is the number of vertices that belong to cell C.

III. APPLICATION TO THE VERTEX MODEL WITH DIFFERENT TYPES OF DISSIPATION

In this section, we applied the normal mode formalism to analyze the linear viscoelastic properties of the vertex model of epithelial tissues with both external and internal dissipation mechanisms. The results were compared against direct numerical simulations of the vertex model. In the vertex model, a confluent epithelial tissue is represented as a polygonal tiling of the plane subject to periodic boundary conditions. Two cells share a junction, which is assumed to be a straight line, and three or more cells meet at a vertex, which is the degree of freedom in the model. The mechanical energy of the system is given by the following energy function,

$$E = \sum_C \left[\frac{K}{2} (A_C - A_0)^2 + \frac{\Gamma}{2} (P_C - P_0)^2 \right], \qquad (18)$$

where K and Γ are the area and perimeter moduli, and A_C and P_C are the actual area and perimeter of cell C, respectively. In this work, we assumed all the cells have the same preferred areas A_0 and preferred perimeters P_0. The dimensionless cell-shape parameter $p_0 = P_0/\sqrt{A_0}$ controls whether the model tissue is in the solid or the fluid regime [30]. Model tissues with low (high) values of the cell-shape parameters $p_0 < p_c$ ($p_0 > p_c$) behave like solids (fluids). The critical value of the cell-shape parameter p_c that characterizes the solid-fluid transition is $p_c = \sqrt{8\sqrt{3}} \approx 3.722$ for regular hexagonal tilings [47], while for disordered tilings the critical value falls in the range $p_c \approx 3.8 - 3.9$ [30, 38, 48] and depends on the procedure with which they are generated. Here, we consider both regular hexagonal and disordered tilings. Expressions for mechanical forces $-\nabla_{\mathbf{R}_i} E$ on each vertex, the Hessian matrix $\hat{\boldsymbol{H}}$, and $\bar{\mathbf{f}}^{\mathrm{pb}}$ that are used for the normal modes analysis are given in Appendices A, B, and C, respectively.

The dynamics of the vertex model has been studied almost exclusively with the assumption that the only source of dissipation is the interaction between the vertex and the substrate [49]. In real epithelial tissues, however, there are different sources of dissipation, many of which have not been well understood. We, therefore, implemented three types of dissipation mechanisms, as shown in Fig. 2. These are encoded in the matrix $\hat{\boldsymbol{C}}$ and describe the dynamics of vertices [see Eq. (1)]. Specifically, Fig. 2a shows the friction $f_i^d = -\gamma \mathbf{V}_i$ due to the relative velocity $\mathbf{V}_i$ between the vertex i and the substrate. In this case, the dissipation matrix takes a simple diagonal form, $\hat{\boldsymbol{C}} = \gamma \hat{\boldsymbol{I}}$, where γ is the friction coefficient and $\hat{\boldsymbol{I}}$ is the identity matrix. In Fig. 2b, we consider the internal dissipation due to relative motions of neighboring vertices with friction coefficient ζ_V. In this case, the dissipation force for the vertex i can be expressed as $f_i^d = -\zeta_V \sum_{j_\alpha \in S_i} (\mathbf{V}_i - \mathbf{V}_{j_\alpha})$, where the summation runs over all nearest neighbor vertices, which are indicated as the "star" of vertex i denoted with the set $\mathcal{S}_i$. Since each vertex is shared by three cell-cell junctions, $3\zeta_V$ appears on the diagonal of the $\hat{\boldsymbol{C}}$ matrix and each row has three nonzero off-diagonal elements with the value $-\zeta_V$. Another formulation of the internal dissipation is to consider the relative motions of neighboring cells, as shown in Fig. 2c. The velocity of the cell C, $\mathbf{V}_C = \frac{1}{N_C} \sum_{i \in C} \mathbf{V}_i$, is defined as the average velocity of the N_C vertices that belong to it. $\mathbf{f}_C^d = -\zeta_C \sum_{C_n \in \mathcal{N}_C} (\mathbf{V}_C - \mathbf{V}_{C_n})$ is the friction force that cell C experiences due to the relative motions with respect to its neighboring cells with friction coefficient ζ_C, where $\mathcal{N}_C$ includes all neighboring cells of cell C. This friction force is assumed to be equally distributed across all the vertices that belong to the cell C. The total friction force on vertex i is denoted as $\mathbf{f}_i^d = \sum_{C \in \mathcal{N}_i} \frac{\mathbf{f}_C^d}{N_C}$. Once friction force at each vertex is known, the dissipation matrix $\hat{\boldsymbol{C}}$ can be written accordingly. Note that in this dissipation model, more than three vertices contribute to the force on a given vertex each contributing to an off-diagonal element of the matrix $\hat{\boldsymbol{C}}$. We conclude by noting that the models characterizing internal dissi-

pation, such as the ones in Fig. 2b,c, play an important role if cells are not supported by substrate, e.g., as it is the case in early-stage embryos.

In the remainder of this section, we show how the three different types of dissipation described above affect the rheological properties of the vertex model for regular hexagonal and disordered tilings. For all scenarios, we compared the results of the normal mode analysis with direct numerical simulations of the vertex model.

A. Simulation setup

We start by briefly summarizing the setup of our vertex model simulations, with additional details provided in Ref. [39]. In most simulations of the vertex model [Eq. (18)], we fixed the value of K, A_0 and measured the energy in units KA_0^2, stresses in units KA_0 and lengths in unit $A_0^{1/2}$. The preferred cell perimeter P_0, was varied to tune the system between solid or fluid phases. We fixed the perimeter modulus Γ by fixing the ratio $KA_0/\Gamma \approx 3.464$ in most simulations since it does not affect the location of the solid to fluid transition. In Fig. 4 we, however, show an example on how the ratio KA_0/Γ affects the dynamic shear modulus by changing the area modulus K.

We created regular hexagonal as well as disordered tilings subject to periodic boundary conditions as described in [39]. All configurations used to probe the rheology correspond to the local energy minimum obtained by the FIRE minimization algorithm [50]. The shear rheology was probed by applying an oscillatory affine simple shear described by the deformation gradient $\hat{\boldsymbol{F}} = \left(\begin{smallmatrix} 1 & \epsilon(t) \\ 0 & 1 \end{smallmatrix}\right)$, where $\epsilon(t) = \epsilon_0 \sin(\omega_0 t)$ and we used a small magnitude of deformation, i.e., $\epsilon = 10^{-7}$. At each time step, we first applied the affine shear deformation to the simulation box and all vertices, which was followed by internal relaxation of vertices according to the overdamped dynamics [see Eq. (1)].

The response stress tensor, $\hat{\boldsymbol{\sigma}}_C(t)$, for each cell C was computed using the formalism introduced in Refs. [51–53] as $\hat{\boldsymbol{\sigma}}_C = -\Pi_C \hat{\boldsymbol{I}} + \frac{1}{2A_C}\sum_{e\in C} \mathbf{T}_e \otimes \mathbf{l}_e$, where the summation is over all junctions e belonging to cell C. Here, $\Pi_C = -\frac{\partial E}{\partial A_C} = -K(A_C - A_0)$ is the hydrostatic pressure inside a cell, $\hat{\boldsymbol{I}}$ is the unit tensor, and $\mathbf{T}_e = \frac{\partial E}{\partial \mathbf{l}_e} = \Gamma(P_C - P_0)\mathbf{l}_e/|\mathbf{l}_e|$ is the tension along the junction e with $\mathbf{l}_e$ being a vector joining the two vertices on it [51–53]. The average stress tensor $\hat{\boldsymbol{\sigma}}(t) = \sum_C w_C \hat{\boldsymbol{\sigma}}_C(t)$, with $w_C = A_C/\sum_C A_C$, was used as a measure for the response of the system. We recorded the average shear stress signal $\hat{\sigma}_{xy}(t)$ once the system reached a steady state. The dynamics modulus $G^*(\omega_0) = \tilde{\hat{\sigma}}_{xy}(\omega_0)/\tilde{\epsilon}(\omega_0)$ was computed at a given driving frequency ω_0 of the applied strain, where $\tilde{\hat{\sigma}}_{xy}(\omega)$ and $\tilde{\epsilon}(\omega)$ are the Fourier transforms of $\hat{\sigma}_{xy}(t)$ and $\epsilon(t)$, respectively.

B. Friction between vertices and a substrate

We first performed simulations of the vertex model with external dissipation only, i.e., the friction force $-\gamma \mathbf{V}_i$ applied to each vertex, as shown in Fig. 2a. We validated the normal mode approach by comparing the shear moduli with the results of simple shear simulations of regular hexagonal tilings, which has been analysed extensively in our previous work [39]. Fig. 3a,b show the storage and loss moduli obtained from simulations (dots) for representative values of p_0 in (a) the solid and (b) the fluid phase, which show excellent agreement with the predictions (lines) of the normal mode analysis. The corresponding eigenvalues λ_k and the normalized coefficients $\bar{\alpha}_k \bar{G}_k = \alpha_k G_k \gamma/(KA_0)^2$ and $\bar{\beta}_k \bar{G}_k = \beta_k G_k/(KA_0)$ for the normal mode analysis are shown in Figs. 3c,d and 3e,f, respectively.

In our previous work [39], we noted that the rheological response of regular hexagonal tilings in the solid and fluid phases can be well described with the standard linear solid and Burgers model, respectively. This can be explained with the help of normal modes. The shear response in the solid phase is dominated by the set of normal modes in the shaded region Fig. 3e with the highest values of coefficients $\bar{\alpha}_k \bar{G}_k$ and $\bar{\beta}_k \bar{G}_k$. These normal modes all correspond to the identical eigenvalue that we denote as λ_D (see shaded region in Fig. 3c). Hence, the shear response of hexagonal tilings in the solid phase is characterized by a single time scale λ_D^{-1}, which can be accurately captured by the standard linear solid model. Note that the response of the system is dominated by the linear combination of normal modes that corresponds to the projection of the affine shear deformation to the set of these degenerate normal modes as $\boldsymbol{\xi}_D = \sum_{k \text{ s.t. } \lambda_k = \lambda_D} \left(\boldsymbol{\xi}_k^{\intercal}\, \mathbf{u}^{\text{aff}}\right) \boldsymbol{\xi}_k$ of the same eigenvalue λ_D. The normal mode $\boldsymbol{\xi}_D$ is shown in the inset of Fig. 3b, where it is represented by the corresponding displacement field, which shows that the connected vertices move horizontally by the same magnitude but in opposite directions.

In the fluid phase (bottom row of Fig. 3), the spectrum of normal modes can be grouped in a region of zero modes ($\lambda_k = 0$) and two distinct regions with approximately constant values of eigenvalues λ_k (two shaded regions in Fig. 3d). These two regions of non-zero modes set the two characteristic timescales (marked with arrows in Fig. 3b) of the shear response of hexagonal tilings in the fluid phase, which can be approximated with the Burgers model. Note that the zero modes do not contribute to the shear response because the value of normalized coefficient $\bar{\alpha}_k \bar{G}_k \approx 0$ (see Fig. 3f).

We used the normal mode approach to further demonstrate how the ratio between the area and perimeter moduli, KA_0/Γ, affects the shear rheology of the vertex model. We measured the storage and loss moduli of disordered tilings with different area modulus K as shown in Fig. 4a,b for two representative values of p_0. The simulation results (symbols) show excellent agreement with

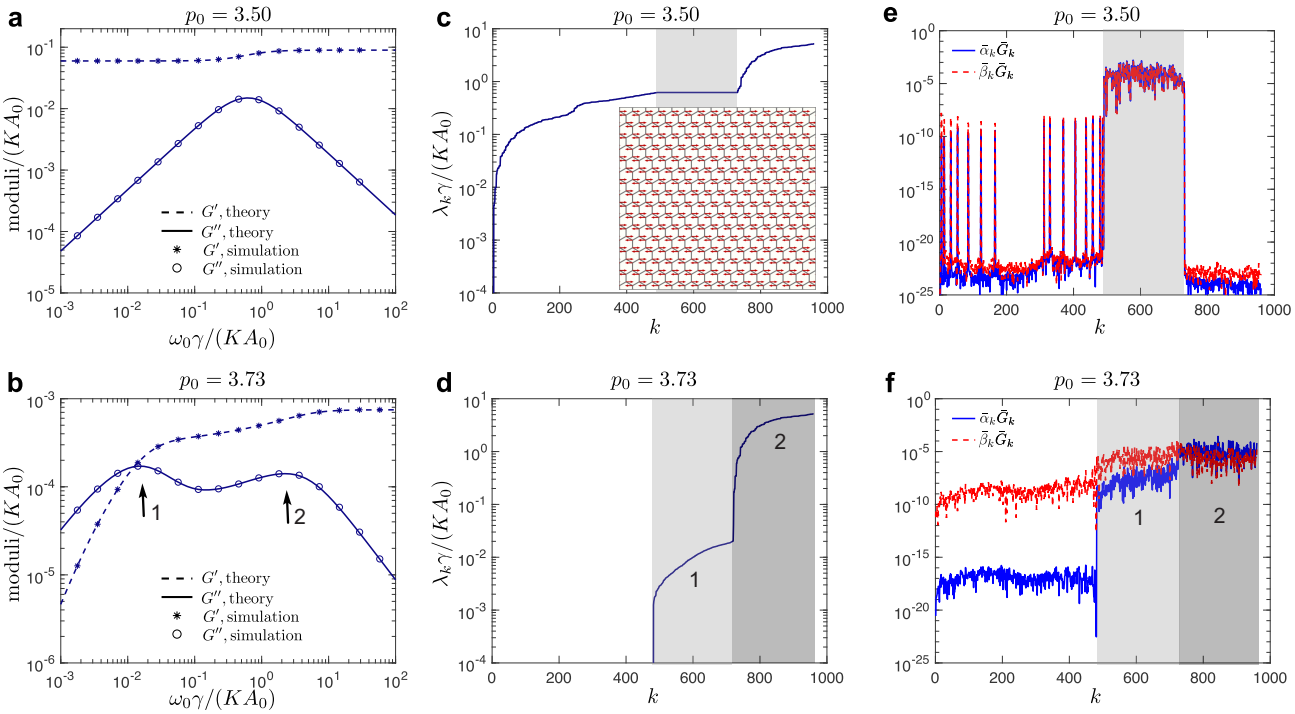

FIG. 3. Shear rheology of hexagonal tilings with dissipation due to friction with the solid substrate. Results for two representative values of the cell shape parameter, $p_0 = 3.5$ in the solid phase (top row) and $p_0 = 3.73$ in the fluid phase (bottom row) are shown. (a,b) Storage and loss moduli from the simulations (symbols) compared with the predictions from normal modes (lines). (c,d) Nonzero eigenvalues λ_k in the ascending order. (e,f) Normalized coefficients $\bar{\alpha}_k\bar{G}_k = \alpha_k G_k\gamma/(KA_0)^2$ and $\bar{\beta}_k\bar{G}_k = \beta_k G_k/(KA_0)$. The inset in (c) shows a schematic of the normal mode $\boldsymbol{\xi}_D$ that dominates the shear rheology of hexagonal tilings in the solid phase. This dominant normal mode is a linear combination of degenerate normal modes within the shaded region in panel (c,e). Labelled arrows in panel (b) denote peaks that correspond to the characteristic timescales from the normal modes in the shaded regions in panels (d) and (f).

the predictions from the normal modes (lines). Note that in Fig. 4 we fixed Γ and measured the stresses in units Γ and time in units γ/Γ. We varied the values of K by two orders of magnitude as indicated by the colorbars for the ratio KA_0/Γ. Fig. 4c,d show the corresponding eigenvalues λ_k in the ascending order. The eigenvalues λ_k for $k > 600$ are strongly affected by the magnitude of the area modulus K. This indicates that the area term in the vertex model in Eq. (18) has a stronger contribution to the normal modes of large eigenvalues, which strongly affects the loss moduli at high frequency as a function of K (see Fig. 4a,b). Fig. 4e,f shows the corresponding coefficients $\bar{\alpha}_k\bar{G}_k$ and $\bar{\beta}_k\bar{G}_k$ at a representative value of $KA_0/\Gamma = 34.641$. In our previous work [39], we noted that the standard linear solid and Burgers model cannot accurately capture the shear rheological properties for disordered tilings in the vicinity of the solid-fluid transition with $p_0 \approx 3.9$. This can be seen in Fig. 4b for $p_0 = 3.87$, where the complex rheological behavior is a consequence of the broad spectrum of normal mode eigenvalues λ_k (see Fig. 4d). This reflects one of the key results in the normal mode approach that the full response of the vertex model is the sum of the contributions from all the normal modes, each of which behaves as a standard linear solid.

C. Friction due to relative motion of neighboring vertices

In this section, we analyse the shear rheology of the vertex model with the internal friction due to relative motion of connected vertices characterized with the friction coefficient ζ_V (see Fig. 2b) in addition to the vertex-substrate friction with the friction coefficient γ (see Fig. 2a). In Fig. 5, we first report the results for hexagonal tilings at representative values of the cell shape parameter in the solid phase (top) and the fluid phase (bottom). Fig. 5a,b show an excellent match between the storage and loss moduli obtained from simulations (symbols) and the theoretical predictions from the normal modes (lines) for various values of the internal friction coefficient ζ_V.

The moduli curves in the solid phase are characterized by a single timescale, and all curves for different values of ζ_V can be collapsed by rescaling the frequency as $\omega_0(\gamma + 6\zeta_V)/(KA_0)$. This is because the shear response is dominated by the normal mode $\boldsymbol{\xi}_D$ introduced in the previous section, which is shown by the single peak of the normalized coefficients $\bar{\alpha}_k\bar{G}_k$ and $\bar{\beta}_k\bar{G}_k$ marked by the arrow in Fig. 5e. The normal mode $\boldsymbol{\xi}_D$ is simultane-

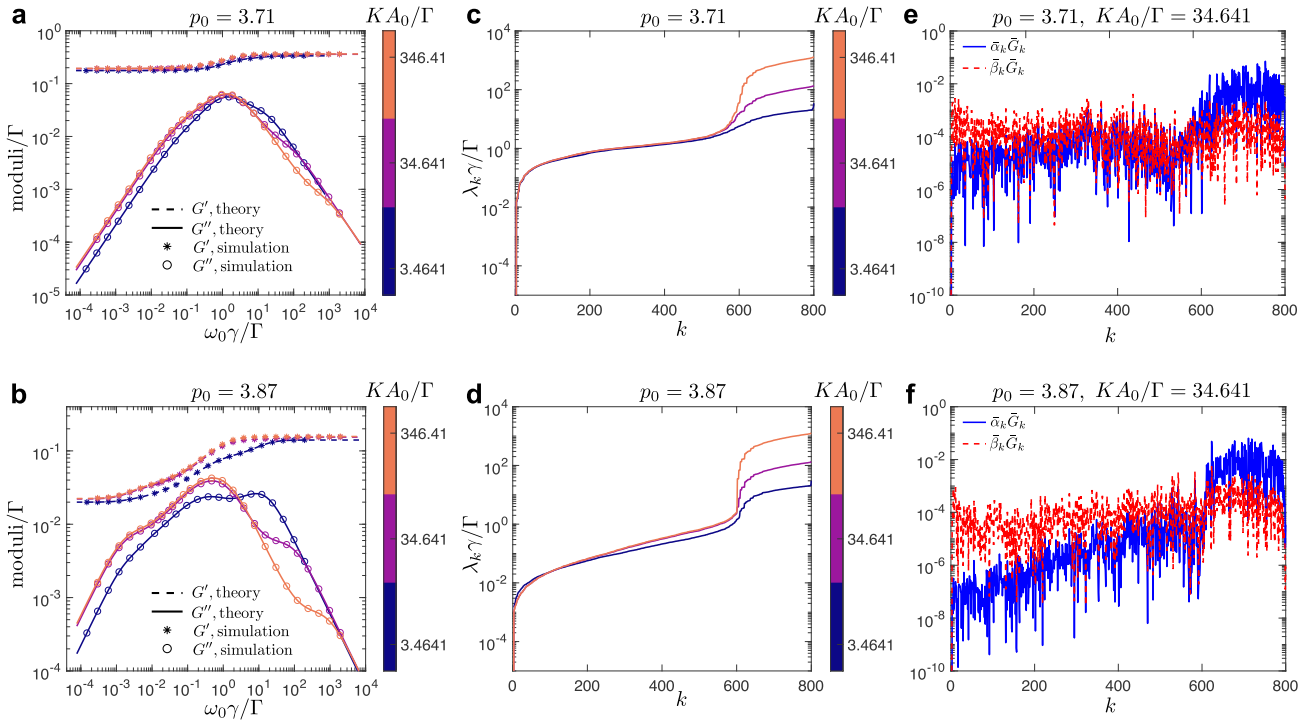

FIG. 4. Shear rheology of disordered tilings with dissipation due to friction with the substrate for different values of the area elastic moduli K. Results for two representative values of the cell shape parameter, $p_0 = 3.71$ (top row) and $p_0 = 3.87$ (bottom row), are shown. (a,b) Storage and loss moduli from the simulations (symbols) compared with the predictions from normal modes (lines). Different colors represent the results from different values of the ratio KA_0/Γ. (c,d) Nonzero eigenvalues λ_k in ascending order for different values of KA_0/Γ. (e,f) Normalized coefficients $\bar{\alpha}_k\bar{G}_k = \alpha_k G_k\gamma/(KA_0)^2$ and $\bar{\beta}_k\bar{G}_k = \beta_k G_k/(KA_0)$ at one representative value of $KA_0/\Gamma = 34.641$.

ously the eigenvector of the Hessian matrix $\hat{\boldsymbol{H}}$ and the dissipation matrix $\hat{\boldsymbol{C}}$. In particular, $\hat{\boldsymbol{C}}\boldsymbol{\xi}_D = (\gamma+6\zeta_V)\boldsymbol{\xi}_D$, since each vertex in the normal mode $\boldsymbol{\xi}_D$ moves in the opposite direction but with the same magnitude as the three vertices connected to it (see the schematic of $\boldsymbol{\xi}_D$ in the inset of Fig. 3c). The eigenvalue $\gamma+6\zeta_V$ with respect to $\hat{\boldsymbol{C}}$ thus accounts for the scaling factor of the frequency in the Fig. 5a.

In the fluid phase, we rescaled the frequency with the same factor to help visually compare the change in the moduli with respect to the friction coefficient ζ_V, as shown in Fig. 5b. As ζ_V increases, the separation of the two peaks in the loss modulus becomes more pronounced. This is consistent with the spectrum of nonzero eigenvalues λ_k shown in Fig. 5e, in which the jump of the eigenvalues between two regions becomes more pronounced as ζ_V increases.

We proceed to perform simulations of the vertex model with disordered tilings, which mimic the geometry of real epithelial tissues. The first column in Fig. 6 shows the storage and loss moduli from simulations (symbols) for representative values of the cell shape parameter deep in the solid phase (top row, $p_0 = 3.06$), close to the solid-fluid transition point on the solid side (middle row, $p_0 = 3.87$), and in the fluid phase (bottom row, $p_0 = 3.99$), which show excellent match with predictions from the normal modes (lines). The frequency is again measured in units of $KA_0/(\gamma + 6\zeta_V)$. When the system is deep in the solid phase, as shown in Fig. 6a, the response is similar to a standard linear solid with loss modulus having one peak. However, the transition region is broader compared to the single standard linear solid model because the corresponding spectrum of normal mode eigenvalues λ_k smoothly increases by an order of magnitude (see Fig. 6d).

When the system is close to the solid-fluid transition on the solid side (see Fig. 6b), the loss modulus develops two peaks, whose separation becomes more pronounced as ζ_V increases. This is similar to the behavior for hexagonal tilings shown in Fig. 5b, which can be accounted for by the sharper jump between the two regions of eigenvalues λ_k with increasing ζ_V, as shown in Figs. 5d and 6e. Furthermore, the loss modulus crosses over from the linear scaling ($\sim \omega$) at low frequencies to anomalous scaling ($\sim \omega^\alpha$) with the fractional exponent $\alpha < 1$ at intermediate frequencies (see Fig. 6b), which was already noted in our prior work in Ref. [39]. This is because the eigenvalues λ_k gradually increase by two orders of magnitude up to the sharp jump point in Fig. 6e

In the fluid phase, the internal dissipation ζ_V has a similar effect on the separation of two peaks in the loss modulus as shown in Fig. 6c. This is also reflected by

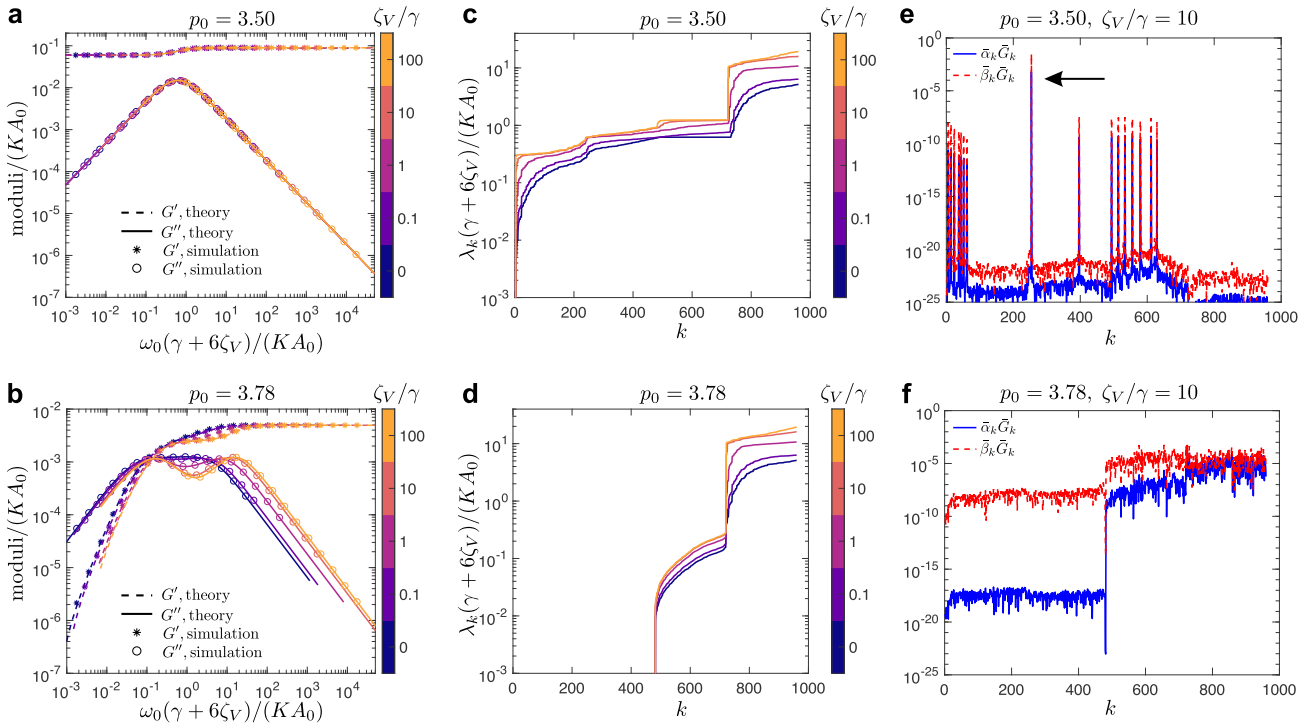

FIG. 5. Shear rheology of hexagonal tilings with internal dissipation due to the relative motion of neighboring vertices in addition to the vertex-substrate friction. Results for two representative values of the cell shape parameter, $p_0 = 3.5$ in the solid phase (top row) and $p_0 = 3.78$ in the fluid phase (bottom row) are shown. (a,b) Storage and loss moduli from the simulations (symbols) compared with the predictions from normal modes (lines) for different values of the internal friction coefficient ζ_V (see colorbar). (c,d) Nonzero eigenvalues λ_k in ascending order for different values of ζ_V. (e,f) Normalized coefficients $\bar{\alpha}_k\bar{G}_k = \alpha_k G_k\gamma/(KA_0)^2$ and $\bar{\beta}_k\bar{G}_k = \beta_k G_k/(KA_0)$ for a representative value of $\zeta_V/\gamma = 10$. In the solid phase, the rheological response is dominated by the single normal mode $\boldsymbol{\xi}_D$ marked by the arrow in panel (e), which corresponds to the highest value of coefficients $\bar{\alpha}_k\bar{G}_k$ and $\bar{\beta}_k\bar{G}_k$.

the sharper jump between two regions of eigenvalues with increasing ζ_V in Fig. 6f.

D. Friction due to relative motions of neighboring cells

Finally, we investigated the shear rheology of the vertex model with the internal friction due to relative motion of neighboring cells characterized with the friction coefficient ζ_C (see Fig. 2c) in addition to the vertex-substrate friction with the friction coefficient γ (see Fig. 2a). We only studied the shear rheology of disordered tilings since the dominant normal mode $\boldsymbol{\xi}_D$ in hexagonal tilings does not generate friction due to relative motion of neighboring cells. Thus, the shear rheology for the hexagonal tilings is similar to the results presented in Fig. 3 with only the cell-substrate friction.

The first column in Fig. 7 shows the storage and loss moduli from simulations (symbols) for representative values of the cell shape parameter deep in the solid phase (top row, $p_0 = 3.06$), close to the solid-fluid transition point on the solid side (middle row, $p_0 = 3.87$), and in the fluid phase (bottom row, $p_0 = 3.99$), which all show excellent match with predictions from the normal modes (lines). For a system deep in the solid phase, the loss modulus develops two peaks from one peak as ζ_C increases (see Fig. 7a), which corresponds to the jump of the eigenvalues λ_k developing at $k \approx 400$ in Fig. 7d.

When the system is close to the solid-fluid transition on the solid side, the range of frequencies over which the loss modulus has a significant value becomes wider with a small bump developing at low frequency as ζ_C increases (see Fig. 7b). This is reflected by a wider range of eigenvalues λ_k with increasing ζ_C in Fig. 7e. This behavior is different from the response of the system with friction due to relative motion of neighboring vertices, for which the dynamic range of characteristic time scales does not significantly change with ζ_V 0 (see Fig. 6b)

In the fluid phase, the two small bumps in the loss modulus when there is only external dissipation (i.e., for $\zeta_C = 0$) are smoothed out as ζ_C increases (see Fig. 7c). This is different from the more pronounced separation of two peaks in the loss modulus for larger dissipation ζ_V due to relative motion of neighboring vertices (see Fig. 6c). This is because the jump of eigenvalues λ_k at $k \approx 600$ is smoothed out with increasing ζ_C as shown in Fig. 7f.

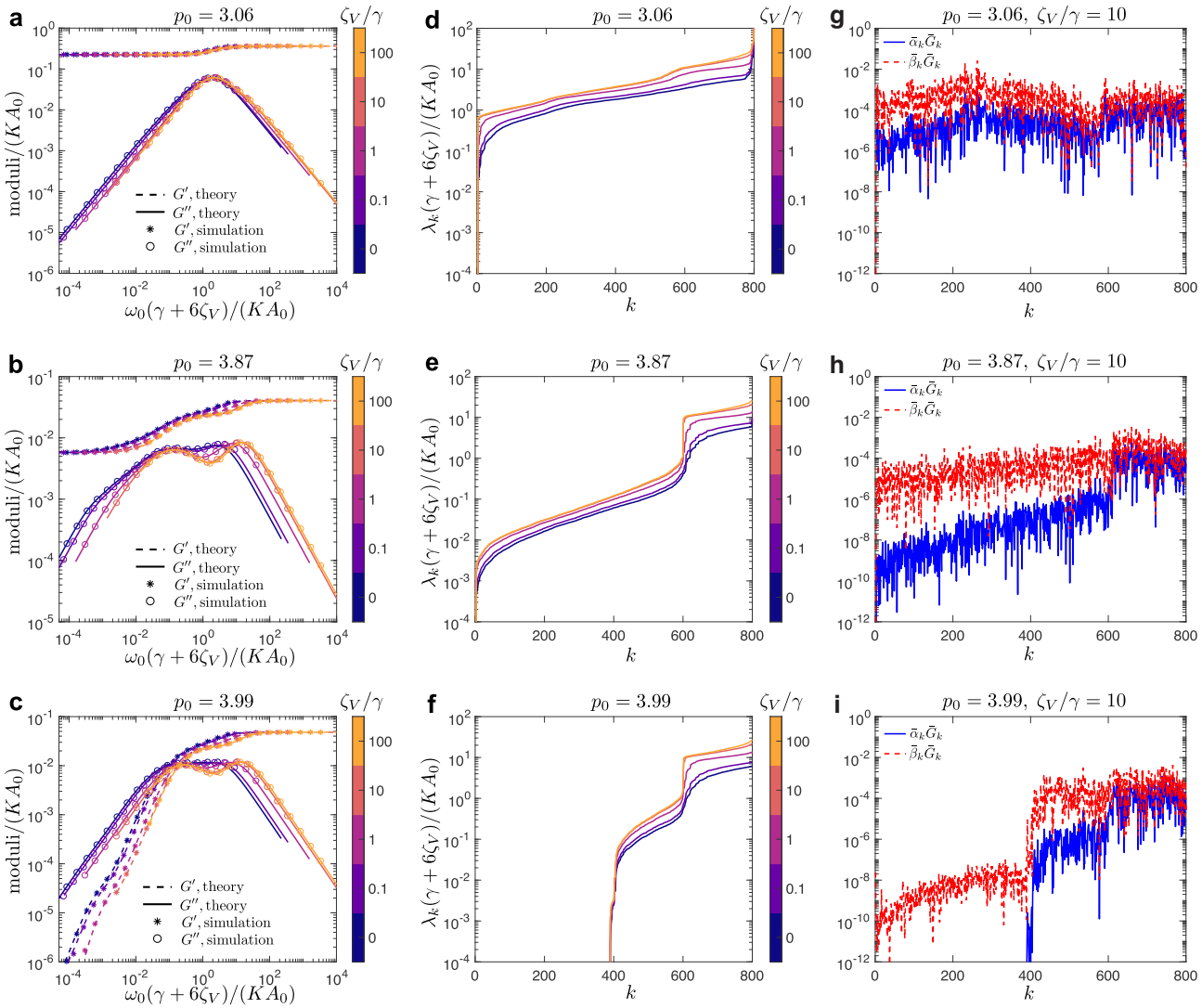

FIG. 6. Shear rheology for disordered tilings with internal dissipation due to relative motion of neighboring vertices in addition to cell-substrate friction. Results for three representative values of the cell shape parameter, $p_0 = 3.06$ deep in the solid phase (first row), $p_0 = 3.87$ close to the solid-fluid transition point on the solid side (second row), $p_0 = 3.99$ in the fluid phase (bottom row) are shown. (a,b,c) Storage and loss moduli from the simulations (symbols) compared with the predictions from normal modes (lines) for different values of the internal friction coefficient ζ_V (see colorbar). (d,e,f) Nonzero eigenvalues λ_k in ascending order for different values of ζ_V. (g,h,i) Normalized coefficients $\bar{\alpha}_k\bar{G}_k = \alpha_k G_k\gamma/(KA_0)^2$ and $\bar{\beta}_k\bar{G}_k = \beta_k G_k/(KA_0)$ for a representative value of $\zeta_V/\gamma = 10$.

IV. DISCUSSION AND CONCLUSIONS

Harmonic approximation of the energy function of a system in the vicinity of a local energy minimum allows one to write the equations of motion in terms of decoupled normal modes, which is a general formalism widely used in physics. In this work, we used the normal mode description to develop a general method for calculating dynamic rheological moduli of soft materials in the linear response regime. The dynamic rheological moduli can be represented as a linear superposition of standard linear solid models with the characteristic timescales related to the corresponding eigenvalues of normal modes. The method is applicable to systems with any number of spatial dimensions as long as it is possible to assign to it an energy function with well-defined local minima and expand it around such a minimum to the second order in terms of displacements. Extension to systems with inertia is straightforward. In addition, the method allows treatment of different microscopic dissipation mechanisms, putting weak restrictions on the specific functional form of the dissipation, e.g., the treatment is limited to dissipation that depends linearly on agent velocities.

We applied the normal modes approach to study the linear response to shear deformations of the vertex model

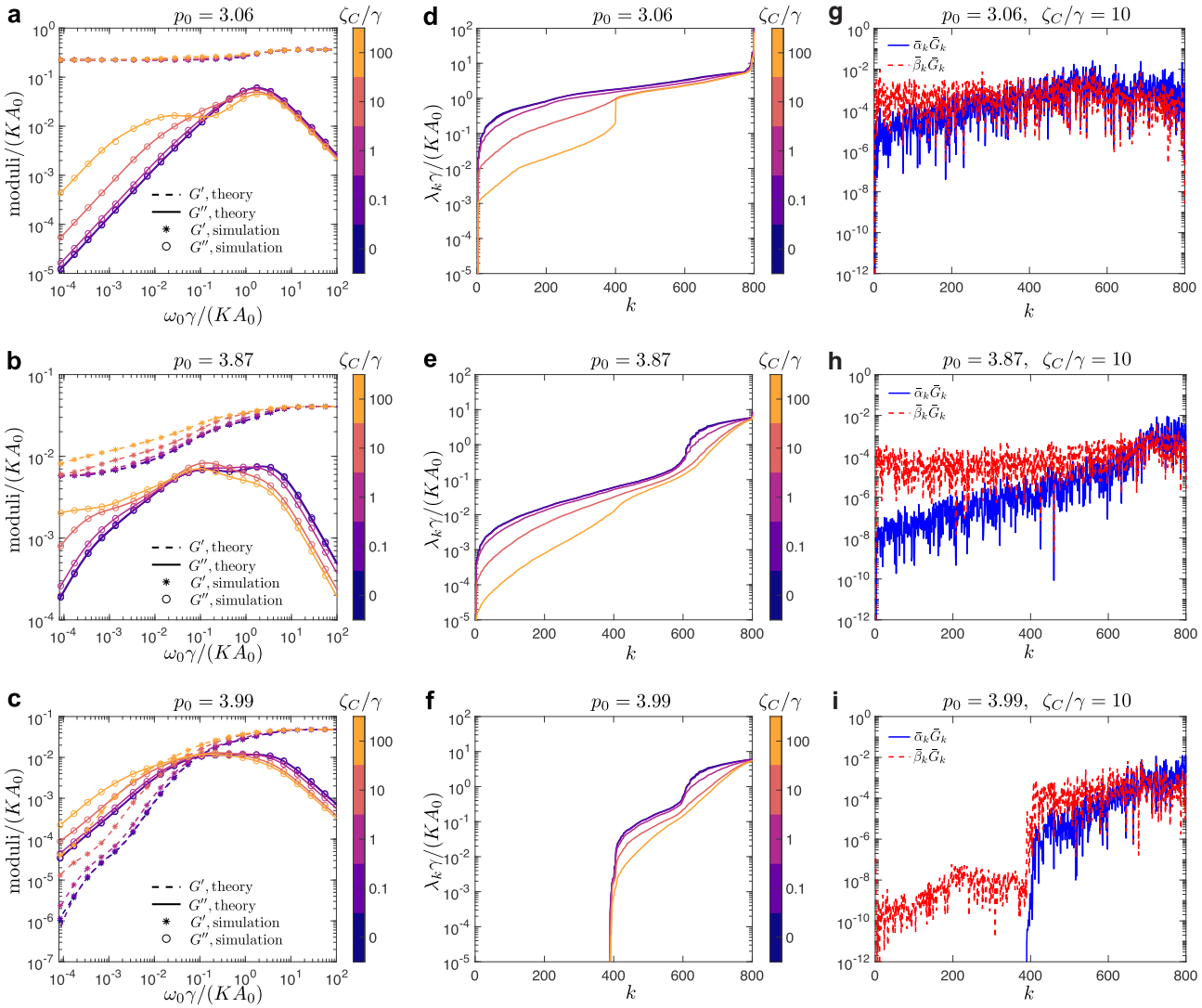

FIG. 7. Shear rheology for disordered tilings with internal dissipation due to relative motion of neighboring cells in addition to cell-substrate friction. Results are shown for three representative values of the cell shape parameter, $p_0 = 3.06$ deep in the solid phase (top row), $p_0 = 3.87$ close to the solid-fluid transition point on the solid side (middle row), and $p_0 = 3.99$ in the fluid phase (bottom row). (a,b,c) Storage and loss moduli from the simulations (symbols) compared with the predictions from normal modes (lines) for different values of the internal friction coefficient ζ_C (see colorbar). (d,e,f) Nonzero eigenvalues λ_k in ascending order for different values of ζ_C. (g,h,i) Normalized coefficients $\bar{\alpha}_k\bar{G}_k = \alpha_k G_k\gamma/(KA_0)^2$ and $\bar{\beta}_k\bar{G}_k = \beta_k G_K/(KA_0)$ at one representative value of $\zeta_C/\gamma = 10$.

for epithelial tissue mechanics with three different microscopic mechanisms dissipation. We have shown that in all three cases, the method gives an excellent agreement with numerical simulations. One of the key findings of this work is that detailed features of the dynamic moduli are very sensitive to the exact form of the internal dissipation. This can have important impact on understanding of the rheology of actual biological tissues in the linear response regime since it shows that the same mechanical model can have very different response depending on the specific form of the microscopic dissipation.

Despite the fact that the normal modes formalism is limited to the linear response regime and is unable to capture the response to large deformations, especially if those involve local plastic rearrangements, it allows one to dissect the linear response of the vertex model and fully understand features of the storage and loss moduli curves as functions of frequency in terms of dominant normal modes. Applying this approach to compute and understand other response functions, e.g., the bulk modulus is also straightforward, as is treatment of different forms of external driving. For example, modeling typical experimental setup where the system is clamped at two of its ends that are then moved relative to each other would just involve introducing the appropriate functional form for the driving force in Eq. (3). Finally, this methods is

far superior in terms of computational cost compared to direct simulations.

ACKNOWLEDGMENTS

This research was primarily supported by NSF through the Princeton University's Materials Research Science and Engineering Center DMR-2011750 and by the Project X Innovation Research Grant from the Princeton School of Engineering and Applied Science (S.T. and A.K.). R.S. acknowledges support by the UK BBSRC (Award BB/N009789/1). This project was initiated during the KITP program "Symmetry, Thermodynamics and Topology in Active Matter" (ACTIVE20), and it is supported in part by the National Science Foundation under Grant No. NSF PHY-1748958.

Appendix A: Force on a vertex

In this appendix we outline the derivation of the expression for the force on the vertex i in the vertex model. The force $\mathbf{F}_i = -\nabla_{\mathbf{R}_i} E$, where E is the energy function of the vertex model given in Eq. (18). We use Latin subscript indices to denote different vertices and Greek superscript indices to denote components of a vector.

Area of the cell C is $A_C = \frac{1}{2}\sum_{i\in C}(\mathbf{R}_i \times \mathbf{R}_{i+1})\cdot \mathbf{N}_C$, where $\mathbf{N}_C \equiv \mathbf{e}_z$ is the unit-length vectors perpendicular to the plane of the tissue. In terms of components, we have

$$A_C = \frac{1}{2}\sum_{i\in C} \varepsilon_{\alpha\beta\gamma} R_i^\alpha R_{i+1}^\beta N_C^\gamma. \tag{A1}$$

$\varepsilon_{\alpha\beta\gamma}$ is the Levi-Civita symbol and summation over repeated Greek indices is implied. Similarly, the perimeter of cell C is

$$\begin{aligned} P_C &= \sum_{i\in C} |\mathbf{R}_{i+1} - \mathbf{R}_i| \\ &= \sum_{i\in C} \left[\left(R_{i+1}^\alpha - R_i^\alpha\right)\left(R_{i+1}^\alpha - R_i^\alpha\right)\right]^{1/2}, \end{aligned} \tag{A2}$$

where the sum loops over all n vertices i that belong to the cell C, and $i+1 > n$ corresponds to the first vertex, i.e., $i = 1$.

The force is then

$$\mathbf{F}_i = -\sum_{[C]} \left[K\left(A_C - A_0\right)\nabla_{\mathbf{R}_i} A_C + \Gamma\left(P_C - P_0\right)\nabla_{\mathbf{R}_i} P_C\right], \tag{A3}$$

where $[C]$ means that the sum is only over cells that contain vertex i. It is easy to show that

$$\nabla_{\mathbf{R}_i} A_C = \frac{1}{2}\left(\mathbf{R}_{i+1,i} - \mathbf{R}_{i,i-1}\right)\times \mathbf{N}_C, \tag{A4}$$

and

$$\nabla_{\mathbf{r}_i} P_C = \frac{\mathbf{R}_{i,i-1}}{|\mathbf{R}_{i,i-1}|} - \frac{\mathbf{R}_{i+1,i}}{|\mathbf{R}_{i+1,i}|}, \tag{A5}$$

where $\mathbf{R}_{i+1,i} \equiv \mathbf{R}_{i+1} - \mathbf{R}_i$, etc.

If one loops over all cell-cell junctions that contain vertex i is the counterclockwise direction, each vertex connected to i by a junction will belong to two neighboring cells. However, in the cell to the right of the junction (when looking away from vertex i) the neighboring vertex will appear as $i-1$ and in the cell to the left of the junction as $i+1$. If we mark cell to the right as C_1 and cell to the left as C_2 and the vertex connected to vertex i by the junction between cells C_1 and C_2 as $\mathbf{R}_j$, then the contribution to the force will be

$$\begin{aligned} &\frac{K}{2}\left(A_{C_1} - A_0\right)\mathbf{R}_{j,i}\times\mathbf{e}_z - \frac{K}{2}\left(A_{C_2} - A_0\right)\mathbf{R}_{j,i}\times\mathbf{e}_z = \\ &= -\frac{K}{2}\left(A_{C_1} - A_{C_2}\right)\mathbf{e}_z \times \mathbf{R}_{j,i}, \end{aligned} \tag{A6}$$

and

$$\begin{aligned} &-\Gamma\left(P_{C_1} - P_0\right)\frac{\mathbf{R}_{i,j}}{|\mathbf{R}_{i,j}|} + \Gamma\left(P_{C_2} - P_0\right)\frac{\mathbf{R}_{j,i}}{|\mathbf{R}_{j,i}|} = \\ &= -\Gamma\left(\Delta P_{C_1} + \Delta P_{C_2}\right)\frac{\mathbf{R}_{i,j}}{|\mathbf{R}_{i,j}|}, \end{aligned} \tag{A7}$$

where $\Delta P_{C_i} = (P_{C_i} - P_0)$. Inserting Eqs. (A6) and (A7) into Eq. (A3) one obtains an expression that is very simple to implement numerically,

$$\begin{aligned} \mathbf{F}_i = &-\sum_{j\in\mathcal{S}(i)} \frac{K}{2}\left(A_{C_1} - A_{C_2}\right)\mathbf{e}_z\times\mathbf{R}_{j,i} \\ &+ \sum_{j\in\mathcal{S}(i)} \Gamma\left(\Delta P_{C_1} + \Delta P_{C_2}\right)\hat{\mathbf{R}}_{j,i}, \end{aligned} \tag{A8}$$

where the $j-$sum loops in the counterclockwise order over all vertices $j \in \mathcal{S}(i)$ connected to the vertex i, and $\hat{\mathbf{R}}_{j,i} = \frac{\mathbf{R}_{j,i}}{|\mathbf{R}_{j,i}|}$.

Appendix B: Hessian matrix of the vertex model

In this appendix we outline the derivation of the expressions for the Hessian matrix of the vertex model. To allow for the most general case, we express the energy of the vertex model as

$$E = \sum_C \frac{K_C}{2}\left(A_C - A_0^C\right)^2 + \sum_C \frac{\Gamma_C}{2} P_C^2 - \sum_{\langle ij\rangle} \Lambda_{ij} l_{ij}, \tag{B1}$$

where Λ_{ij} is the line tension and l_{ij} is the length of the junction connecting vertices i and j. $\langle \dots \rangle$ denotes all pairs of vertices connected by junctions. In the case when parameters K_C, Γ_C, A_0^C, and P_0^C are not cell-specific, one immediately reads off $P_0 = \frac{\Lambda}{\Gamma}$ and readily recovers Eq. (18).

For a system with N vertices, the Hessian of the vertex model is a real symmetric matrix of size $2N \times 2N$. Its elements are

$$H_{IJ} = \left.\frac{\partial^2 E}{\partial x_I \partial x_J}\right|_{\mathbf{r}=\mathbf{r}^{\rm eq}}, \tag{B2}$$

where $I, J \in \{1, \ldots, 2N\}$, and $I = 2(i-1)+\alpha$, with $i \in \{1, \ldots, N\}$ and $\alpha \in \{1, 2\}$. In other words, for $I = 2i-1$, $x_I \equiv R_i^x$ and for $I = 2i$, $x_I \equiv R_i^y$. Identical relations hold for index J. Elements of the Hessian matrix are calculated for a configuration in mechanical equilibrium, i.e., for $\mathbf{r} = \mathbf{r}^{\rm eq}$. One finds,

$$\frac{\partial^2 E}{\partial R_k^\alpha \partial R_m^\beta} = \sum_C K_C \frac{\partial A_C}{\partial R_k^\alpha}\frac{\partial A_C}{\partial R_m^\beta} + \sum_C K_C \left(A_C - A_0^C\right)\frac{\partial^2 A_C}{\partial R_k^\alpha \partial R_m^\beta} + \sum_C \Gamma_C \frac{\partial P_C}{\partial R_k^\alpha}\frac{\partial P_C}{\partial R_m^\beta} + \sum_C \Gamma_C P_C \frac{\partial^2 P_C}{\partial R_k^\alpha \partial R_m^\beta} - \sum_{\langle ij\rangle} \Lambda_{ij}\frac{\partial^2 l_{ij}}{\partial R_k^\alpha \partial R_m^\beta}. \tag{B3}$$

The expression for $\frac{\partial A_C}{\partial R_k^\alpha}$ is given in Eq. (A4) and the expression for $\frac{\partial P_C}{\partial R_k^\alpha}$ in Eq. (A5). It is straightforward to show that

$$\frac{\partial^2 A_C}{\partial R_k^\alpha \partial R_m^\beta} = \frac{1}{2}\varepsilon_{\beta\alpha 3}\delta_{m+1,k} - \frac{1}{2}\varepsilon_{\beta\alpha 3}\delta_{m-1,k}, \tag{B4}$$

where, as usual, we assumed that the cells are in the $xy-$plane. Similarly,

$$\frac{\partial P_C^2}{\partial R_k^\alpha \partial R_m^\beta} = -\frac{\left(R_m^\alpha - R_{m-1}^\alpha\right)\left(R_m^\beta - R_{m-1}^\beta\right)}{\left|\mathbf{R}_m - \mathbf{R}_{m-1}\right|^3}\left(\delta_{m,k} - \delta_{m-1,k}\right) + \frac{\left(\delta_{m,k} - \delta_{m-1,k}\right)\delta_{\alpha\beta}}{\left|\mathbf{R}_m - \mathbf{R}_{m-1}\right|} + \frac{\left(R_{m+1}^\beta - R_m^\beta\right)\left(R_{m+1}^\alpha - R_m^\alpha\right)}{\left|\mathbf{R}_{m+1} - \mathbf{R}_m\right|^3}\left(\delta_{m+1,k} - \delta_{m,k}\right) - \frac{\left(\delta_{m+1,k} - \delta_{m,k}\right)\delta_{\alpha\beta}}{\left|\mathbf{R}_{m+1} - \mathbf{R}_m\right|}. \tag{B5}$$

Finally,

$$\frac{\partial^2 l_{ij}}{\partial R_k^\alpha \partial R_m^\beta} = -\frac{\left(R_i^\beta \delta_{im} - R_i^\beta \delta_{jm} - R_j^\beta \delta_{im} + R_j^\beta \delta_{jm}\right)}{l_{ij}^3}\left(R_i^\alpha - R_j^\alpha\right)\left(\delta_{i,k} - \delta_{j,k}\right) + \frac{\delta_{\alpha\beta}}{l_{ij}}\left(\delta_{ik}\delta_{im} - \delta_{ik}\delta_{jm} - \delta_{jk}\delta_{im} + \delta_{jk}\delta_{jm}\right). \tag{B6}$$

Appendix C: External driving force due to shear of the periodic simulation box in the vertex model

In this appendix we outline the derivation of the expression for the external driving force $\bar{\mathbf{f}}^{\rm pb}$ due to shear of the periodic simulation box in the vertex model. We use the energy function for the vertex model given in Eq. (B1) and seek to find the expression for

$$\bar{f}_I^{\rm pb} = -\frac{\partial^2 E}{\partial x_I \partial \epsilon}\Big|_{\mathbf{r}=\mathbf{r}^{\rm eq},\epsilon=0}, \tag{C1}$$

Similarly as in the derivation of the Hessian matrix given in the previous appendix, one finds

$$\frac{\partial^2 E}{\partial R_k^\alpha \partial \epsilon} = \sum_C K_C \frac{\partial A_C}{\partial R_k^\alpha}\frac{\partial A_C}{\partial \epsilon} + \sum_C K_C \left(A_C - A_0^C\right)\frac{\partial^2 A_C}{\partial R_k^\alpha \partial \epsilon} + \sum_C \Gamma_C \frac{\partial P_C}{\partial R_k^\alpha}\frac{\partial P_C}{\partial \epsilon} + \sum_C \Gamma_C P_C \frac{\partial^2 P_C}{\partial R_k^\alpha \partial \epsilon} - \sum_{\langle ij\rangle} \Lambda_{ij}\frac{\partial^2 l_{ij}}{\partial R_k^\alpha \partial \epsilon}. \tag{C2}$$

The shear degree of freedom ϵ only shows up in the distance vectors that cross the periodic boundary of the box with size $\ell_x \times \ell_y$. In other words, the energy of the vertex model depends on ϵ through the x-component of the distance vectors

$$R_{m,n}^x = R_n^x - R_m^x + q_{m,n}^x \ell_x + \epsilon q_{m,n}^y \ell_y, \tag{C3}$$

where $q^x_{m,n} = 0$ if vertices m and n are connected without crossing the right/left boundary, $q^x_{m,n} = +1(-1)$ if the distance vector going from vertex m to vertex n crosses the right (left) boundary and analogous for $q^{m,n}_y$ in terms of top/bottom boundary [36]. The derivative with respect to ϵ is

$$\frac{\partial}{\partial \epsilon} = \sum_{\langle m,n \rangle} q^y_{m,n} \ell_y \frac{\partial}{\partial R^x_{m,n}} \tag{C4}$$

It is straightforward to show that

$$\frac{\partial A_C}{\partial \epsilon} = \frac{1}{2} \sum_j R^y_{1,j+1} \ell_y q^y_{1,j} - R^y_{1,j} \ell_y q^y_{1,j+1}, \tag{C5}$$

where 1 in the subscript denoted an arbitrarily chosen first vertex in the cell C. Similarly,

$$\frac{\partial P_C}{\partial \epsilon} = \sum_{\langle m,n \rangle} q^y_{m,n} \ell_y \frac{1}{|\mathbf{R}_{m,n}|} R^x_{m,n}, \tag{C6}$$

$$\frac{\partial^2 A_C}{\partial R^\alpha_k \partial \epsilon} = \sum_{\langle m,n \rangle \in C} q^y_{m,n} \ell_y (\delta_{m,k}\delta_{n,k+1} + \delta_{m,k-1}\delta_{n,k}) \delta_{\alpha,2}, \tag{C7}$$

$$\begin{aligned} \frac{\partial^2 P_C}{\partial R^\alpha_k \partial \epsilon} = \sum_{\langle m,n \rangle \in C} q^y_{m,n} \ell_y (& - \frac{R^\alpha_{k-1,k} R^x_{k-1,k}}{|\mathbf{R}_{k-1,k}|^3} \delta_{m,k-1}\delta_{n,k} + \frac{\delta_{m,k-1}\delta_{n,k}\delta_{\alpha 1}}{|\mathbf{R}_{k-1,k}|} \\ & + \frac{R^\alpha_{k,k+1} R^x_{k,k+1}}{|\mathbf{R}_{k,k+1}|^3} \delta_{m,k}\delta_{n,k+1} - \frac{\delta_{m,k}\delta_{n,k+1}\delta_{\alpha 1}}{|\mathbf{R}_{k,k+1}|}), \end{aligned} \tag{C8}$$

and

$$\begin{aligned} \frac{\partial^2 l_{ij}}{\partial R^\alpha_k \partial \epsilon} &= q^y_{m,n} \ell_y \frac{\partial^2 l_{ij}}{\partial R^\alpha_k \partial R^x_{m,n}} \\ &= q^y_{m,n} \ell_y \left(- \frac{\left(R^\alpha_{i,j}\delta_{ik} - R^\alpha_{i,j}\delta_{jk} \right)}{l^3_{ij}} R^x_{i,j} \delta_{i,m}\delta_{j,n} + \frac{\delta_{\alpha 1}}{l_{ij}} \left(\delta_{im}\delta_{jn}\delta_{ik} - \delta_{im}\delta_{j,n}\delta_{jk} \right) \right). \end{aligned} \tag{C9}$$

[1] R. G. Larson, *The Structure and Rheology of Complex Fluids*, Vol. 150 (Oxford University Press New York, 1999).

[2] M. Doi, *Soft Matter Physics* (Oxford University Press, 2013).

[3] M. Doi, S. F. Edwards, and S. F. Edwards, *The Theory of Polymer Dynamics*, Vol. 73 (oxford university press, 1988).

[4] T. Mason, J. Bibette, and D. Weitz, Elasticity of compressed emulsions, Phys. Rev. Lett. **75**, 2051 (1995).

[5] P. Sollich, F. Lequeux, P. Hébraud, and M. E. Cates, Rheology of soft glassy materials, Phys. Rev. Lett. **78**, 2020 (1997).

[6] P. Sollich, Rheological constitutive equation for a model of soft glassy materials, Phys. Rev. E **58**, 738 (1998).

[7] L. E. Silbert, A. J. Liu, and S. R. Nagel, Vibrations and diverging length scales near the unjamming transition, Phys. Rev. Lett. **95**, 098301 (2005).

[8] C. S. O'Hern, L. E. Silbert, A. J. Liu, and S. R. Nagel, Jamming at zero temperature and zero applied stress: The epitome of disorder, Phys. Rev. E **68**, 011306 (2003).

[9] N. Xu, V. Vitelli, M. Wyart, A. J. Liu, and S. R. Nagel, Energy transport in jammed sphere packings, Phys. Rev. Lett. **102**, 038001 (2009).

[10] M. Wyart, H. Liang, A. Kabla, and L. Mahadevan, Elasticity of floppy and stiff random networks, Phys. Rev. Lett. **101**, 215501 (2008).

[11] M. Marchetti, J. Joanny, S. Ramaswamy, T. Liverpool, J. Prost, M. Rao, and R. A. Simha, Hydrodynamics of soft active matter, Rev. Mod. Phys. **85**, 1143 (2013).

[12] M. Poujade, E. Grasland-Mongrain, A. Hertzog, J. Jouanneau, P. Chavrier, B. Ladoux, A. Buguin, and P. Silberzan, Collective migration of an epithelial monolayer in response to a model wound, Proc. Natl. Acad. Sci. U.S.A. **104**, 15988 (2007).

[13] X. Trepat, M. R. Wasserman, T. E. Angelini, E. Millet,

D. A. Weitz, J. P. Butler, and J. J. Fredberg, Physical forces during collective cell migration, Nat. Phys. **5**, 426 (2009).

[14] D. T. Tambe, C. C. Hardin, T. E. Angelini, K. Rajendran, C. Y. Park, X. Serra-Picamal, E. H. Zhou, M. H. Zaman, J. P. Butler, D. A. Weitz, *et al.*, Collective cell guidance by cooperative intercellular forces, Nat. Mater. **10**, 469 (2011).

[15] S. Tlili, E. Gauquelin, B. Li, O. Cardoso, B. Ladoux, H. Delanoë-Ayari, and F. Graner, Collective cell migration without proliferation: density determines cell velocity and wave velocity, R. Soc. Open Sci. **5**, 172421 (2018).

[16] A. Saraswathibhatla, S. Henkes, E. E. Galles, R. Sknepnek, and J. Notbohm, Coordinated tractions increase the size of a collectively moving pack in a cell monolayer, Extreme Mech. Lett. **48**, 101438 (2021).

[17] A. Szabó, R. Ünnep, E. Méhes, W. Twal, W. Argraves, Y. Cao, and A. Czirók, Collective cell motion in endothelial monolayers, Phys. Biol. **7**, 046007 (2010).

[18] T. E. Angelini, E. Hannezo, X. Trepat, M. Marquez, J. J. Fredberg, and D. A. Weitz, Glass-like dynamics of collective cell migration, Proc. Natl. Acad. Sci. U.S.A. **108**, 4714 (2011).

[19] T. B. Saw, A. Doostmohammadi, V. Nier, L. Kocgozlu, S. Thampi, Y. Toyama, P. Marcq, C. T. Lim, J. M. Yeomans, and B. Ladoux, Topological defects in epithelia govern cell death and extrusion, Nature **544**, 212 (2017).

[20] S. Henkes, K. Kostanjevec, J. M. Collinson, R. Sknepnek, and E. Bertin, Dense active matter model of motion patterns in confluent cell monolayers, Nat. Commun. **11**, 1 (2020).

[21] A. R. Harris, L. Peter, J. Bellis, B. Baum, A. J. Kabla, and G. T. Charras, Characterizing the mechanics of cultured cell monolayers, Proc. Natl. Acad. Sci. U.S.A. **109**, 16449 (2012).

[22] A. Bonfanti, J. Fouchard, N. Khalilgharibi, G. Charras, and A. Kabla, A unified rheological model for cells and cellularised materials, R. Soc. Open Sci. **7**, 190920 (2020).

[23] A. Bonfanti, J. L. Kaplan, G. Charras, and A. Kabla, Fractional viscoelastic models for power-law materials, Soft Matter **16**, 6002 (2020).

[24] A. Nicolas, E. E. Ferrero, K. Martens, and J.-L. Barrat, Deformation and flow of amorphous solids: Insights from elastoplastic models, Rev. Mod. Phys. **90**, 045006 (2018).

[25] N. W. Ashcroft and N. D. Mermin, *Solid State Physics* (Holt-Saunders, 1976).

[26] G. Pessot, H. Löwen, and A. M. Menzel, Dynamic elastic moduli in magnetic gels: Normal modes and linear response, J. Chem. Phys. **145**, 104904 (2016).

[27] H. Honda and G. Eguchi, How much does the cell boundary contract in a monolayered cell sheet?, J. Theor. Biol. **84**, 575 (1980).

[28] R. Farhadifar, J.-C. Röper, B. Aigouy, S. Eaton, and F. Jülicher, The influence of cell mechanics, cell-cell interactions, and proliferation on epithelial packing, Curr. Biol. **17**, 2095 (2007).

[29] A. G. Fletcher, J. M. Osborne, P. K. Maini, and D. J. Gavaghan, Implementing vertex dynamics models of cell populations in biology within a consistent computational framework, Prog. Biophys. Mol. Biol. **113**, 299 (2013).

[30] D. Bi, J. Lopez, J. M. Schwarz, and M. L. Manning, A density-independent rigidity transition in biological tissues, Nat. Phys. **11**, 1074 (2015).

[31] J.-A. Park, J. H. Kim, D. Bi, J. A. Mitchel, N. T. Qazvini, K. Tantisira, C. Y. Park, M. McGill, S.-H. Kim, B. Gweon, *et al.*, Unjamming and cell shape in the asthmatic airway epithelium, Nat. Mater. **14**, 1040 (2015).

[32] N. I. Petridou and C.-P. Heisenberg, Tissue rheology in embryonic organization, EMBO J. **38**, e102497 (2019).

[33] P.-F. Lenne and V. Trivedi, Sculpting tissues by phase transitions, Nat. Commun. **13**, 664 (2022).

[34] D. Bi, X. Yang, M. C. Marchetti, and M. L. Manning, Motility-driven glass and jamming transitions in biological tissues, Phys. Rev. X **6**, 021011 (2016).

[35] D. L. Barton, S. Henkes, C. J. Weijer, and R. Sknepnek, Active vertex model for cell-resolution description of epithelial tissue mechanics, PLOS Comput. Biol. **13**, e1005569 (2017).

[36] M. Merkel and M. L. Manning, A geometrically controlled rigidity transition in a model for confluent 3d tissues, New J. Phys. **20**, 022002 (2018).

[37] M. Moshe, M. J. Bowick, and M. C. Marchetti, Geometric frustration and solid-solid transitions in model 2d tissue, Phys. Rev. Lett. **120**, 268105 (2018).

[38] M. Merkel, K. Baumgarten, B. P. Tighe, and M. L. Manning, A minimal-length approach unifies rigidity in underconstrained materials, Proc. Natl. Acad. Sci. U.S.A. **116**, 6560 (2019).

[39] S. Tong, N. K. Singh, R. Sknepnek, and A. Kosmrlj, Linear viscoelastic properties of the vertex model for epithelial tissues, arXiv preprint arXiv:2102.11181 (2021).

[40] J. Huang, J. O. Cochran, S. M. Fielding, M. C. Marchetti, and D. Bi, Shear-driven solidification and nonlinear elasticity in epithelial tissues, arXiv preprint arXiv:2109.10374 (2021).

[41] M. Popović, V. Druelle, N. A. Dye, F. Jülicher, and M. Wyart, Inferring the flow properties of epithelial tissues from their geometry, New J. Phys. **23**, 033004 (2021).

[42] A. Das, S. Sastry, and D. Bi, Controlled neighbor exchanges drive glassy behavior, intermittency, and cell streaming in epithelial tissues, Phys. Rev. X **11**, 041037 (2021).

[43] B. N. Parlett, *The Symmetric Eigenvalue Problem* (SIAM, 1998).

[44] E. Lerner, G. Düring, and M. Wyart, A unified framework for non-brownian suspension flows and soft amorphous solids, Proc. Natl. Acad. Sci. U.S.A. **109**, 4798 (2012).

[45] E. Lerner, G. Düring, and M. Wyart, Simulations of driven overdamped frictionless hard spheres, Comput. Phys. Commun. **184**, 628 (2013).

[46] M. E. Gurtin, E. Fried, and L. Anand, *The Mechanics and Thermodynamics of Continua* (Cambridge University Press, 2010).

[47] D. Staple, R. Farhadifar, J.-C. Röper, B. Aigouy, S. Eaton, and F. Jülicher, Mechanics and remodelling of cell packings in epithelia, Eur. Phys. J. E **33**, 117 (2010).

[48] X. Wang, M. Merkel, L. B. Sutter, G. Erdemci-Tandogan, M. L. Manning, and K. E. Kasza, Anisotropy links cell shapes to tissue flow during convergent extension, Proc. Natl. Acad. Sci. U.S.A. **117**, 13541 (2020).

[49] A. G. Fletcher, M. Osterfield, R. E. Baker, and S. Y. Shvartsman, Vertex models of epithelial morphogenesis, Biophysical Journal **106**, 2291 (2014).

[50] E. Bitzek, P. Koskinen, F. Gähler, M. Moseler, and P. Gumbsch, Structural relaxation made simple, Phys.

Rev. Lett. **97**, 170201 (2006).
[51] K. K. Chiou, L. Hufnagel, and B. I. Shraiman, Mechanical stress inference for two dimensional cell arrays, PLoS Comput Biol **8**, e1002512 (2012).
[52] X. Yang, D. Bi, M. Czajkowski, M. Merkel, M. L. Manning, and M. C. Marchetti, Correlating cell shape and cellular stress in motile confluent tissues, Proc. Natl. Acad. Sci. U.S.A. **114**, 12663 (2017).
[53] A. Nestor-Bergmann, G. Goddard, S. Woolner, and O. E. Jensen, Relating cell shape and mechanical stress in a spatially disordered epithelium using a vertex-based model, Math. Med. Biol. **35**, i1 (2018).